

Star Formation and Gas Accretion in Nearby Galaxies

Kijeong Yim^{1,2*} and J. M. van der Hulst¹

¹*Kapteyn Astronomical Institute, University of Groningen, P.O. Box 800, 9700 AV Groningen, The Netherlands*

²*Korea Astronomy and Space Science Institute, 776 Daedeok-daero, Yuseong-gu, Daejeon 34055, Korea*

Accepted XXX. Received YYY; in original form ZZZ

ABSTRACT

In order to quantify the relationship between gas accretion and star formation, we analyse a sample of 29 nearby galaxies from the WHISP survey which contains galaxies with and without evidence for recent gas accretion. We compare combined radial profiles of FUV (*GALEX*) and IR 24 μm (*Spitzer*) characterizing distributions of recent star formation with radial profiles of CO (IRAM, BIMA, or CARMA) and H I (WSRT) tracing molecular and atomic gas contents to examine star formation efficiencies in symmetric (quiescent), asymmetric (accreting), and interacting (tidally disturbed) galaxies. In addition, we investigate the relationship between star formation rate and H I in the outer discs for the three groups of galaxies. We confirm the general relationship between gas surface density and star formation surface density, but do not find a significant difference between the three groups of galaxies.

Key words: galaxies: ISM — galaxies: kinematics and dynamics — stars: formation

1 INTRODUCTION

It has long been suggested that gas accretion plays an important role in ongoing star formation in galaxies (e.g., Larson et al. 1980; Sancisi et al. 2008; Sánchez Almeida et al. 2014). In addition, numerical simulations (e.g., Dekel et al. 2009; Brooks et al. 2009) predict a positive correlation between gas accretion and star formation. The importance of gas accretion in galaxies has been demonstrated by many studies. For example, the gas consumption problem (Larson et al. 1980; Kennicutt 1983) can be cured by continuous accretion (Frernali & Tomasetti 2012; Sancisi et al. 2008). Likewise, the constant star formation rate in the Milky Way (e.g., Twarog 1980; Binney et al. 2000) can be explained by gas accretion. The accreted gas originates from the intergalactic medium (IGM) or is gas removed from galaxies by gravitational interactions with companion galaxies. The accreted gas could replenish atomic hydrogen consumed by star formation. However, the correlation between gas accretion and star formation is not straightforward (Sancisi et al. 2008).

Indications for gas accretion are considered to be the presence of extra-planar gas (Oosterloo et al. 2007a; Wakker et al. 2008), warped layers (Ostriker & Binney 1989), and lopsided discs (Bournaud et al. 2005; van Eymeren et al. 2011a). Since H I observations provide possible evidence for gas accretion (e.g., van der Hulst & Sancisi 2004; Oosterloo et al. 2007b), H I observations are expected to be a crucial key revealing the role of accretion. Asymmetric structure and kinematics in H I have been investigated by many authors (e.g., Swaters et al. 2002; Noordermeer et al. 2005; van Eymeren et al. 2011a). Sancisi et al. (2008) found that about half of the galaxies in the Westerbork H I

Survey of Irregular and SPiral galaxies (WHISP; Kamphuis et al. 1996; van der Hulst et al. 2001) show asymmetries in the distribution and/or kinematics of the H I.

The star formation law (or Kennicutt-Schmidt law; Kennicutt 1998) has been investigated in numerous galaxies (e.g., Wong & Blitz 2002; Leroy et al. 2008; Bigiel et al. 2008). The power-law correlation between star formation rate (SFR) and total gas (H I + H₂) or molecular gas (H₂) suggests that star formation is strongly correlated with the gas. We quantify star formation (SF) properties in 29 galaxies with resolved H I, CO, UV and IR data to investigate whether SF characteristics are the same everywhere or depend on interactions and accretion. We can measure the SFR accurately using resolved *GALEX* and *Spitzer* maps and directly show how much the measured SFR is related with the gas properties in different environment such as quiescent, accreting, and tidally disturbed galaxies. The *GALEX* FUV and *Spitzer* 24 μm data have proved to be good SFR indicators (Calzetti et al. 2007; Leroy et al. 2008) and the FUV emission has been detected even in several outer discs (Thilker et al. 2007) while the 24 μm emission is limited to the optical radius (r_{25}). Since H I emission is extended out to $2 \times r_{25}$ or more and the H I gas in the outer regions can be used as a proxy for the accreting gas, the comparison of FUV and H I in these regions will provide the most direct examination for the role of gas accretion in star formation. In order to investigate whether gas accretion and interaction affect the star formation rate (SFR), we divide the galaxies into three groups: quiescent, accreting, and interacting. We consider kinematical and morphological asymmetries as an indication for accretion and the presence of nearby companions as an indication of interactions. The remaining galaxies are symmetric and isolated.

This paper is organized as follows. Section 2 describes our sample selection and the observations. Section 3 shows how the

* E-mail: kyim@kasi.re.kr

sample of galaxies is classified into symmetric, asymmetric, and interacting galaxies based on kinematics and morphology. Section 4 presents the results: radial distributions of Σ_{SFR} , Σ_{H_2} , Σ_{HI} , and Σ_{gas} in Section 4.1, scaled radial distributions in Section 4.2, comparisons between the SFR and gas in the inner regions in Section 4.3 and the outer regions in Section 4.4, and a comparison of all these properties in relation to the stellar mass of the galaxies in Section 4.5. Section 5 summarizes and concludes this work.

2 SAMPLE AND OBSERVATIONAL DATA

2.1 Galaxy Sample

Since spatially resolved data are crucial for comparing star formation and gas properties, we have selected our sample based on availability of resolved data: H I from the WHISP survey (van der Hulst et al. 2001), CO from the IRAM HERACLES survey (Leroy et al. 2009), the IRAM NUGA survey (García-Burillo et al. 2003; Combes et al. 2009), the BIMA SONG survey (Helfer et al. 2003), and the CARMA STING survey (PI: Alberto Bolatto; Rahman et al. 2011; Wong et al. 2013), FUV from *GALEX*, and IR 24 μm from *Spitzer*. Additional selection criteria are good S/N in H I and CO and a galaxy inclination of 70° or less. This resulted in an initial sample of 16 galaxies. Later, we increased the sample with 13 more galaxies that satisfy all criteria except the availability of CO imaging. The final sample of galaxies is listed in Table 1. The galaxy class is determined from the H I kinematics as well as the H I morphology. More details are given in Section 3.

2.2 FUV and IR 24 μm

Most of the FUV emission is produced by the young O and B stars. The fraction absorbed by the dust surrounding the stars is re-emitted in the infrared, so the combination (FUV+24 μm) is a good method to estimate the total recent star formation (Leroy et al. 2008).

We have used FUV maps from the *GALEX* archive. They were taken from the Nearby Galaxy Survey (NGS; Gil de Paz et al. 2007), the All-Sky Imaging Survey (AIS), and the Deep Imaging Survey (DIS). In the FUV images, foreground sources around galaxies are masked and the sky background mean, obtained from several regions far away from a galaxy, has been subtracted. The FUV maps have a spatial resolution of 4.3'' and are in units of counts $\text{s}^{-1} \text{ pixel}^{-1}$, where 1 count s^{-1} (cps) is 108 μJy (equivalent to $1.4 \times 10^{-15} \text{ erg s}^{-1} \text{ cm}^{-2} \text{ \AA}^{-1}$) according to the *GALEX* Observer's Guide. These units have been converted to MJy sr^{-1} to match the *Spitzer* 24 μm data. For the Galactic extinction correction, we have adopted the extinction $A_{\text{FUV}} = 8.24E(B-V)$ given by Wyder et al. (2007), where the $E(B-V)$ values are obtained from the IDL code and the dust maps provided by Schlegel et al. (1998). We used *Spitzer* 24 μm maps from the SINGS survey (Kennicutt et al. 2003), Program ID 59 (PI: G. Rieke), Program ID 69 (PI: G. Fazio), Program ID 3124 (PI: D. Alexander), Program ID 3247 (PI: C. Struck), Program ID 30443 (PI: G. Rieke), Program ID 40204 (PI: R. Kennicutt), and Program ID 50639 (PI: C. Danforth). We downloaded the Basic Calibrated Data (BCD) from the Spitzer Heritage Archive and used MOPEX (Mosaicking and Point Source Extraction) for background matching and mosaicking the BCD images after removing instrumental artifacts using the Image Reduction and Analysis Facility (IRAF) tasks IMSTAT and

IMARITH. The resolution and units of the maps are 5.9'' and MJy sr^{-1} , respectively. In the case of galaxies with AGN (UGC 7030, 7166, and 7989), the central regions (~ 1 kpc) are blanked to reduce the contamination by AGN activity.

2.3 H I and CO

For the total gas properties, we use H I and CO data with the inclusion of helium (a factor of 1.36). The H I data are obtained from the WHISP archive (van der Hulst et al. 2001). There are three kinds of resolutions available in the archive: 12'' \times 12''/sin δ (full resolution), 30'' \times 30'' and 60'' \times 60'' (see Swaters et al. 2002 for details of the reduction process). We have downloaded the highest resolution (12'' \times 12''/sin δ) images as this is closest to the resolutions of the FUV and IR 24 μm images used for determining the SFR. The downloaded images are masked maps in Westerbork Units (1 W.U. = 5 mJy Beam $^{-1}$) reduced by the WHISP pipeline. We converted them to the integrated intensity maps in units of Jy Beam $^{-1}$ km s^{-1} by multiplying the velocity channel separation using the MIRIAD task MATHS.

In order to obtain CO data at sufficiently high resolution and sensitivity, we use CO integrated intensity maps from large single dish or interferometric studies: the IRAM HERACLES survey (Leroy et al. 2009), the IRAM NUGA survey (García-Burillo et al. 2003; Combes et al. 2009), the BIMA SONG survey (Helfer et al. 2003), and the CARMA STING survey (PI: Alberto Bolatto; Rahman et al. 2011; Wong et al. 2013). All the galaxies with CO data are indicated by their telescope in Table 1.

3 HI CLASSIFICATION

Asymmetries of galaxies in their morphology and kinematics have been studied for many decades (e.g., Baldwin et al. 1980; Richter & Sancisi 1994; van Eymeren et al. 2011a, 2011b). In those studies, they found that typically about a half of the galaxies shows asymmetries, suggesting that asymmetric galaxies are very normal (e.g., Richter & Sancisi 1994; Sancisi et al. 2008). Although the origin of the asymmetries has not been established so far, some studies suggested that the asymmetric features might be caused by gas accretion (e.g., Bournaud et al. 2005; Mapelli et al. 2008; Sancisi et al. 2008) or interactions with companions (Jog 1997; Zaritsky & Rix 1997). Based on these studies, we assume that mild asymmetries represent gas accretion, and that strong asymmetries represent interactions. Note, however, that there are also internal mechanisms such as an asymmetric halo potential that can produce asymmetries, which we can not distinguish easily at present. We also looked at the 3.6 μm IR distributions for asymmetries and found that in all but two cases both the H I and the IR distributions are asymmetric, the H I in general being more distorted. The two exceptions are UGC 7256 and UGC 7989, which are symmetric in the IR but not the H I.

We have examined the H I distributions (galaxy morphology), integrated H I profiles, position-velocity (p-v) diagrams, and velocity fields of the galaxies and divided our sample into three groups: symmetric, asymmetric, and interacting galaxies based on the criteria mentioned above. Examples of symmetric, asymmetric and interacting galaxies are presented in Figure 1. In order to show the classification more distinctly in the figure, we used the smoothed version (30'') instead of the highest resolution images that we use for this study. During this classification, we found an intermediate class between symmetric and asymmetric features, so we clas-

Table 1. Galaxy Sample

Galaxy (1)	Distance (Mpc) (2)	$\log\left(\frac{M_*}{M_\odot}\right)$ (3)	H I total flux (Jy km s ⁻¹) (4)	r ₂₅ (arcsec) (5)	Inclination (°) (6)	V _{sys} (km s ⁻¹) (7)	Galaxy Class (8)	CO Telescope (9)
UGC 1913 (NGC 925)	9.3	10.07	326	314	54 ^v	554	A/S	IRAM
UGC 2455 (NGC 1156)	6.5	9.28	64	99	52 ^v	375	S	
UGC 3334 (NGC 1961)	56.0	11.61	75	137	47 ^L	3934	I	IRAM
UGC 3851 (NGC 2366)	3.9	8.44	274	244	68 ^v	99	A	
UGC 4165 (NGC 2500)	9.8	9.35	36	87	28 ^{ES}	504	S	
UGC 4274 (NGC 2537)	8.1	9.32	20	52	33 ^M	452	S	
UGC 4305	5.0	8.76	253	238	40 ^R	142	A	
UGC 4862 (NGC 2782)	39.5	10.84	7	104	30 ^W	2543	I	
UGC 5079 (NGC 2903)	7.3	10.55	277	378	64 ^v	550	S	IRAM
UGC 5532 (NGC 3147)	43.0	11.57	32	117	35 ^v	2814	S	CARMA
UGC 5557 (NGC 3184)	10.1	10.28	123	222	21 ^H	592	A/S	BIMA
UGC 5789 (NGC 3319)	13.3	9.67	94	185	62 ^v	742	A/S	
UGC 5840 (NGC 3344)	6.9	9.91	186	212	18 ^E	588	S	
UGC 6537 (NGC 3726)	17.0	10.70	101	185	49 ^v	864	A/S	BIMA
UGC 6856 (NGC 3938)	15.5	10.44	86	161	24 ^H	808	S	BIMA
UGC 6869 (NGC 3949)	15.8	10.18	45	87	57 ^L	800	A/S	CARMA
UGC 7030 (NGC 4051)	12.9	10.21	44	157	41 ^H	704	S	BIMA
UGC 7166 (NGC 4151)	20.0	10.41	72	189	20 ^N	999	S	CARMA
UGC 7256 (NGC 4203)	22.4	10.89	49	102	51 ^v	1083	A	
UGC 7278 (NGC 4214)	3.8	9.10	260	255	44 ^L	292	S	IRAM
UGC 7323 (NGC 4242)	8.8	9.52	49	150	52 ^v	517	A/S	
UGC 7353 (NGC 4258)	8.0	10.64	509	559	66 ^v	454	S	BIMA
UGC 7524 (NGC 4395)	3.8	9.02	310	395	47 ^v	318	A	
UGC 7651 (NGC 4490)	9.2	10.17	252	189	60 ^H	565	I	BIMA
UGC 7766 (NGC 4559)	9.8	9.95	331	321	67 ^v	814	A/S	IRAM
UGC 7831 (NGC 4605)	4.4	9.37	54	173	56 ^E	146	A/S	CARMA
UGC 7853 (NGC 4618)	8.8	9.21	67	125	36 ^O	537	I	
UGC 7989 (NGC 4725)	26.8	11.46	145	321	44 ^v	1208	A	IRAM
UGC 12754 (NGC 7741)	12.5	9.73	53	131	49 ^v	752	S	

Columns : (1) Galaxy name; (2) distance adopted from the NED database for $H = 73 \text{ km s}^{-1} \text{ Mpc}^{-1}$; (3) total stellar mass (M_*); (4) H I total flux obtained from the masked integrated intensity map using the MIRIAD task HISTO; (5) optical radius r₂₅ from RC3 (de Vaucouleurs et al. 1991); (6) inclination adopted from ^vvan Eymeren et al. (2011a), ^LLEDA, ^NNoordermeer (2006), ^{ES}Elmegreen & Salzer (1999), ^MMatthews & Uson (2008), ^SSwaters (1999), ^WWong et al. (2013), ^HHelper et al. (2003), ^EEpinat et al. (2008), ^OOdewahn (1991); (7) heliocentric systemic velocity adopted from LEDA or NED; (8) galaxy class defined from the H I kinematics and morphology.

sified the intermediate galaxies as A/S. Our classification is presented in Table 1. When comparing with the previous studies by van Eymeren et al. (2011a, 2011b) for galaxies in common, our classification is generally consistent with their results.

4 RESULTS

In order to compare the SFR and the gas surface densities, we first brought all the images to the same resolution using the MIRIAD task CONVOL and then obtained radial profiles of FUV, IR 24 μm, CO, and H I using the Groningen Image Processing System (GIPSY; van der Hulst et al. 1992) task ELLINT. In the case of interacting galaxies, the galaxy merging with UGC 7651 and the tidal tail of UGC 4862 are masked before deriving the surface densities. All the radial profiles are corrected to face-on by multiplying by $\cos i$. The radial sampling is 10'' or 20'' depending on spatial resolution of the object.

4.1 Radial Distributions

The task ELLINT averages the data along tilted rings, so it increases the signal to noise of the measurement. Figure 2 shows

the azimuthally averaged radial profiles of Σ_{SFR} , Σ_{H_2} , Σ_{HI} , and Σ_{gas} for the sub-sample of 16 galaxies for which CO data are available. Figure A1 shows the profiles of Σ_{SFR} and Σ_{HI} for the remaining 13 galaxies in the sample that have no CO data. In order to derive the SFR surface density, we combine FUV and 24 μm radial profiles using the calibration given by Leroy et al. (2008), which is originally based on previous studies (Calzetti et al. 2007; Kennicutt et al. 2007; Salim et al. 2007):

$$\Sigma_{\text{SFR}} [\text{M}_\odot \text{ kpc}^{-2} \text{ yr}^{-1}] = 0.081 I_{\text{FUV}} [\text{MJy sr}^{-1}] + 0.0032 I_{24\mu\text{m}} [\text{MJy sr}^{-1}]. \quad (1)$$

The gas profiles are converted to units of $\text{M}_\odot \text{ pc}^{-2}$ by adopting the standard CO-to-H₂ conversion factor (Strong & Mattox 1996; Dame et al. 2001) and assuming optically thin emission in H I:

$$\Sigma_{\text{H}_2} [\text{M}_\odot \text{ pc}^{-2}] = 3.2 I_{\text{CO}} [\text{K km s}^{-1}], \quad (2)$$

$$\Sigma_{\text{HI}} [\text{M}_\odot \text{ pc}^{-2}] = 0.0146 I_{\text{HI}} [\text{K km s}^{-1}]. \quad (3)$$

The total gas mass is estimated via $1.36(\Sigma_{\text{H}_2} + \Sigma_{\text{HI}})$, where the factor of 1.36 is a correction for helium. All the radial profiles for Σ_{HI} and Σ_{H_2} are shown in Figure 2 (left panels). When we use the HERACLES CO ($J = 2 \rightarrow 1$) data for Σ_{H_2} , we adopt a conversion factor of 0.7 (Leroy et al. 2012) for the line ratio CO(2-

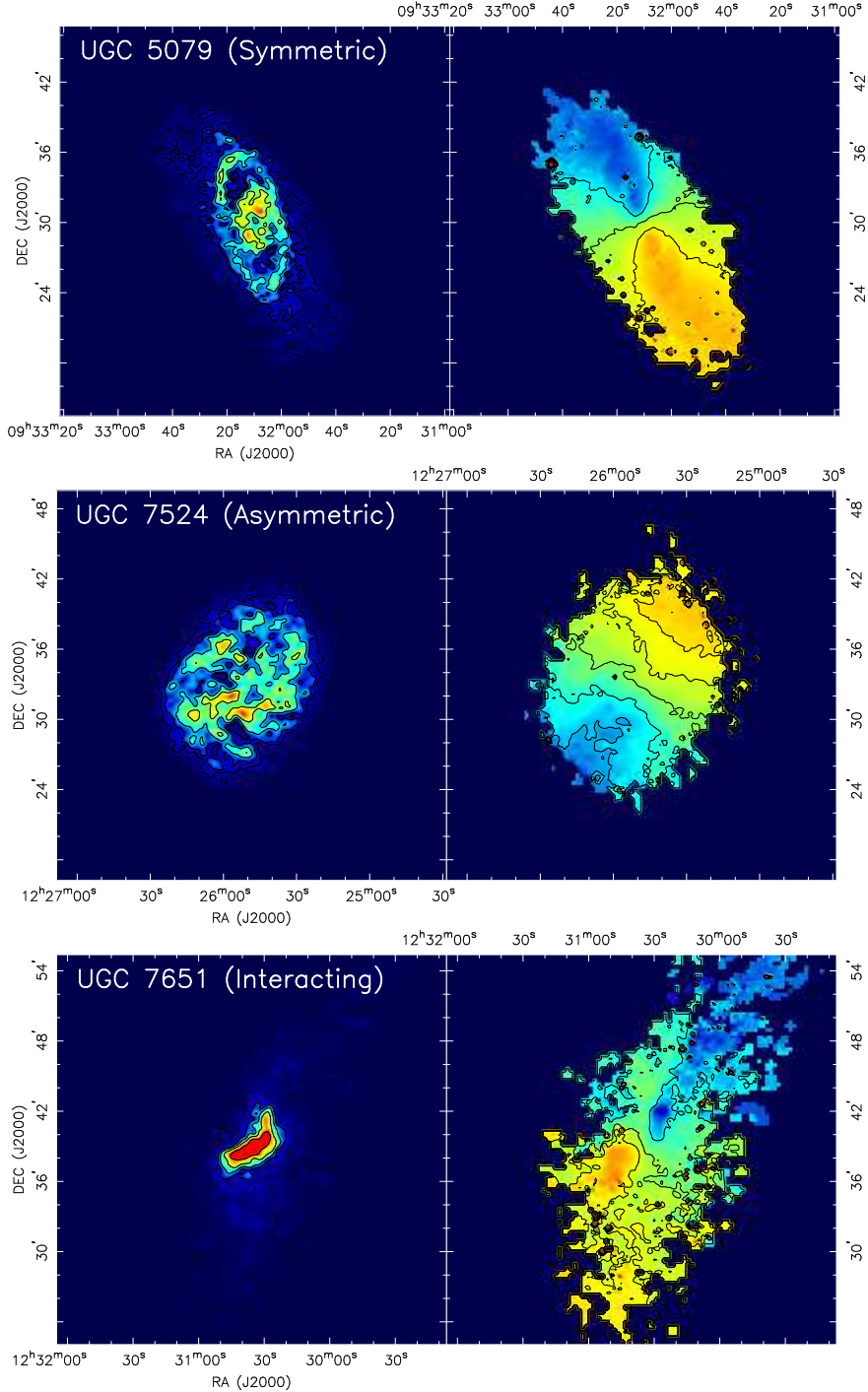


Figure 1. The H I integrated intensity (left panels) and velocity field (right panels) maps for the symmetric (top), asymmetric (middle), and interacting (bottom) galaxies. Left panels: the contours are 0.18×1.78^n mJy Beam $^{-1}$ km s $^{-1}$, with $n=0, 1, 2, 3$ for UGC 5079 (NGC 2903), 0.18×1.78^n mJy Beam $^{-1}$ km s $^{-1}$, with $n=0, 1, 2, 3$ for UGC 7524 (NGC 4395), and 0.84×1.78^n mJy Beam $^{-1}$ km s $^{-1}$, with $n=0, 1, 2, 3$ for UGC 7651 (NGC 4490). The lowest contour is 10% of the peak intensity. Right panels: the contours are 450, 550, and 650 km s $^{-1}$ for UGC 5079 (top), 268, 288, 318, 348, and 368 km s $^{-1}$ for UGC 7524 (middle), and 515, 565, and 605 km s $^{-1}$ for UGC 7651 (bottom).

1)/CO(1–0). The IRAM PdBI CO data for UGC 3334 given by Combes et al. (2009) are not reliable beyond 22'' in radius since the primary beam of PdBI is 43''. Instead, for the outside regions beyond 22'', we have extracted data points from the FCRAO CO profile (Young et al. 1995) using the Dexter tool. The two different data sets match each other well at the radius of 22'' (see the UGC 3334 in the figure). Most galaxies show $\Sigma_{\text{H}_2} > \Sigma_{\text{HI}}$ in the central

regions as expected, but few cases are different (e.g., UGC 1913, UGC 7278, UGC 7651). The galaxies UGC 1913 (NGC 925) and 7278 (NGC 4214) are known as late-type galaxies with faint emission in CO (Leroy et al. 2009) and the galaxy UGC 7651 (NGC 4490) is an irregular galaxy interacting with NGC 4485.

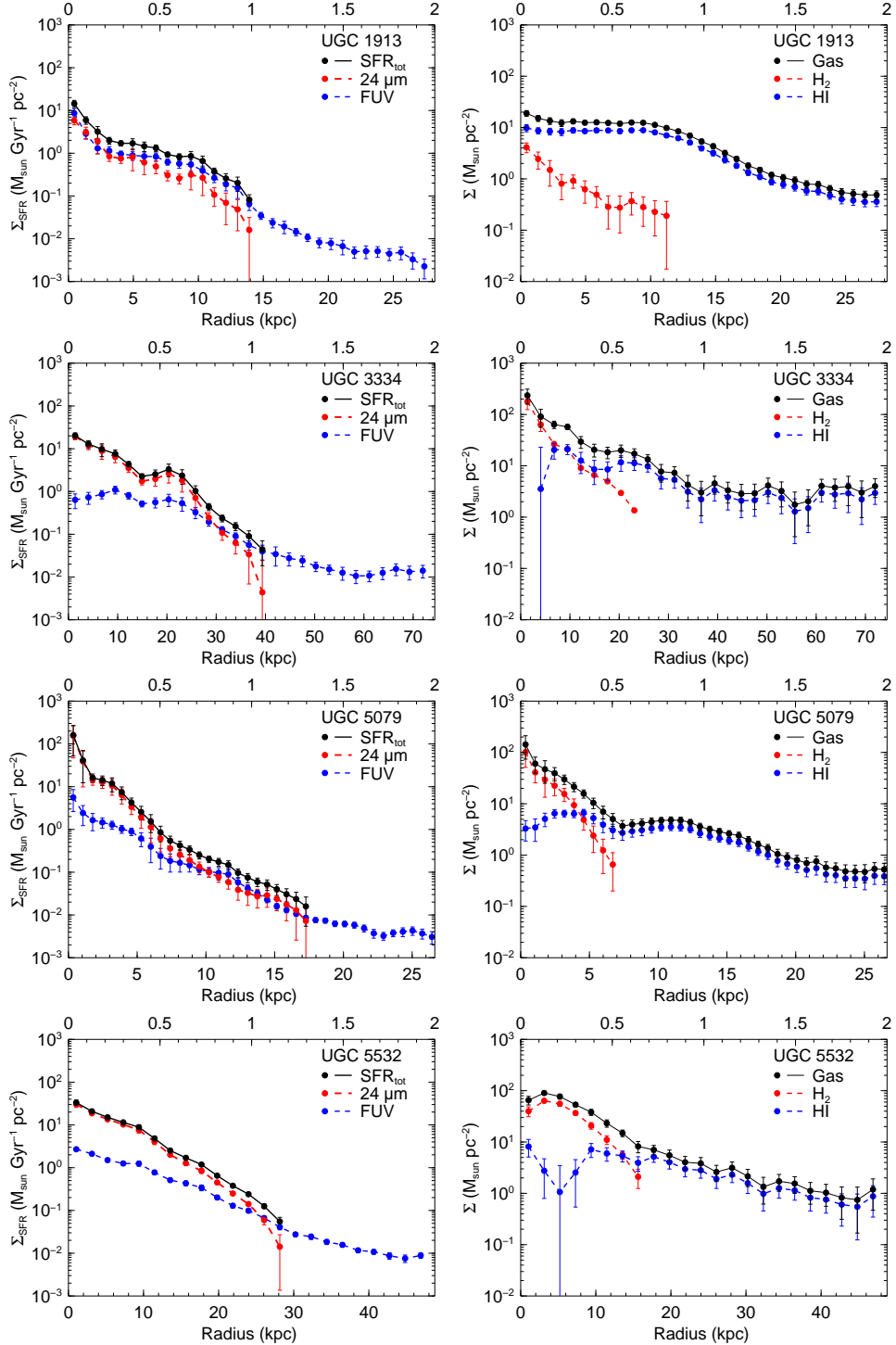


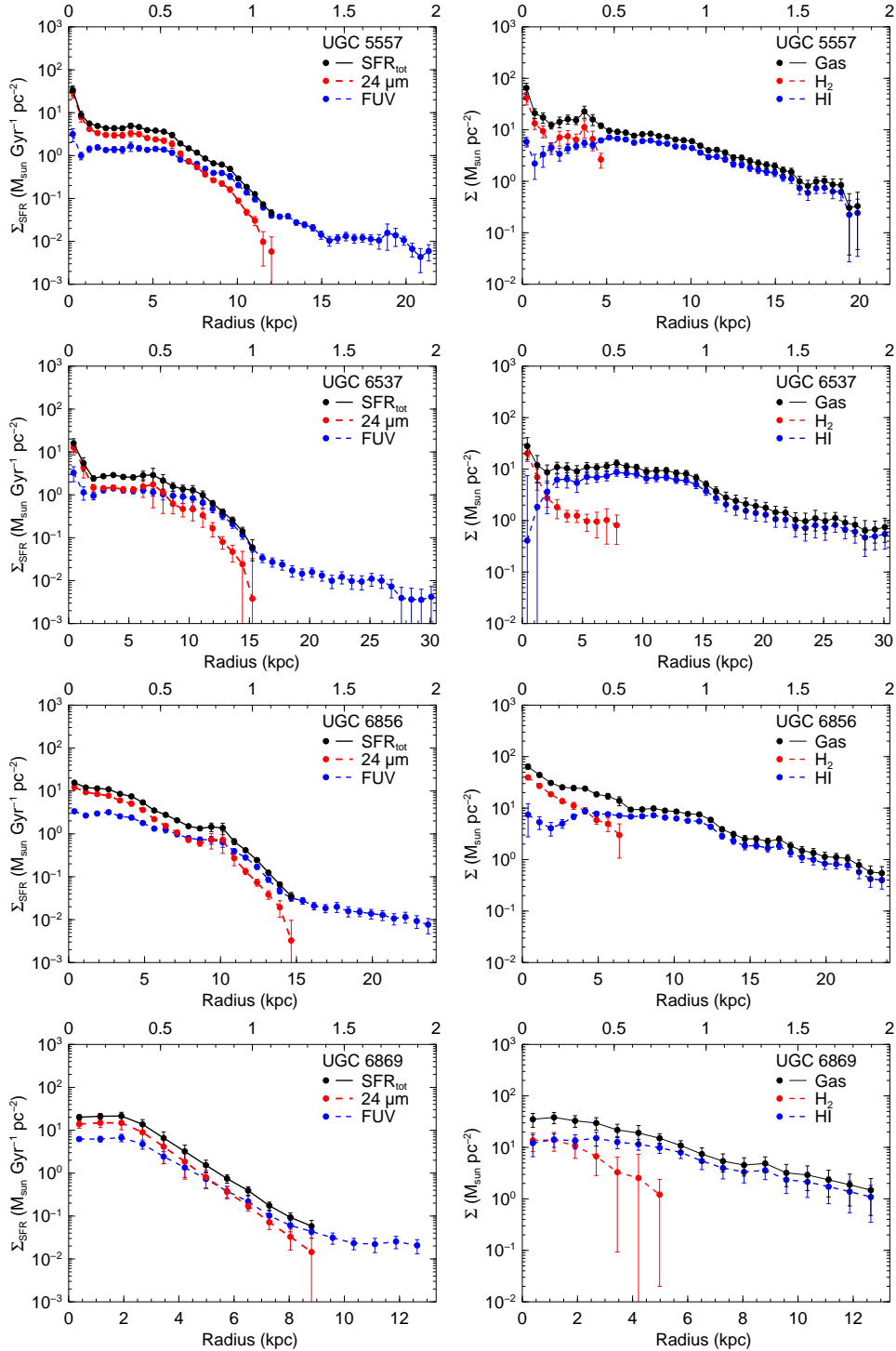
Figure 2. Left panels: radial profiles of $0.081I_{\text{FUV}}$ (blue), $0.0032I_{24\mu\text{m}}$ (red), and the combined Σ_{SFR} (black) given by Equation 1. Right panels: radial profiles of Σ_{H_2} (red), Σ_{HI} (blue), and total gas Σ_{gas} (black). The helium factor (1.36) is included in the total gas: $1.36(\Sigma_{\text{H}_2} + \Sigma_{\text{HI}})$.

4.2 Scaled Radial Profiles

Bigiel & Blitz (2012) found an exponential scaling relation of the total gas ($\Sigma_{\text{HI}} + \Sigma_{\text{H}_2}$) within a factor of two uncertainty from scaled radial profiles of Σ_{gas} for 33 nearby spiral galaxies and the Milky Way. The average profile of the total gas versus normalized radius by r_{25} is well constrained by the exponential fit.

We plot all the scaled radial profiles of Σ_{SFR} , Σ_{H_2} , Σ_{HI} , and

Σ_{gas} for the symmetric (red), intermediate A/S (purple), asymmetric (blue), and interacting (light blue) galaxies in Figure 3. From the figures, we noticed that there is no significant difference between the different types in the scaled radial profiles. We fitted an exponential function to the average values (filled circles) in a bin excluding the central regions. The vertical error bars show the standard deviation of the mean. The Σ_{SFR} and Σ_{H_2} profiles are well fitted by the exponential function, but their scatter is too large. On the

**Figure 2.** continued

other hand, the scatter of Σ_{HI} is relatively small, but it is less well described by the exponential function due to the roughly flat profile within the optical radius. Like the result of Bigiel & Blitz (2012), the exponential fit to the average values of Σ_{gas} for our sample is tightly constrained within a factor of 2 uncertainty (bottom right panel). In order to increase the sample size in the Σ_{gas} profiles, the galaxies without CO data are included only for the outer regions (beyond r_{25}) where Σ_{HI} is dominant. In the bottom right panel,

our exponential fit (solid line) is compared with the universal gas profile (dashed line) given by Bigiel & Blitz (2012):

$$\frac{\Sigma_{\text{gas}}}{\Sigma_{\text{tr}}} = 2.1 \times e^{-1.65 \times r/r_{25}}, \quad (4)$$

here Σ_{tr} is the surface density at the transition radius where $\Sigma_{\text{H}_2} = \Sigma_{\text{HI}}$ and we adopt $14 \text{ M}_{\odot} \text{ pc}^{-2}$ from their study. Note that this value is not obtained from our sample and we only use it for Equa-

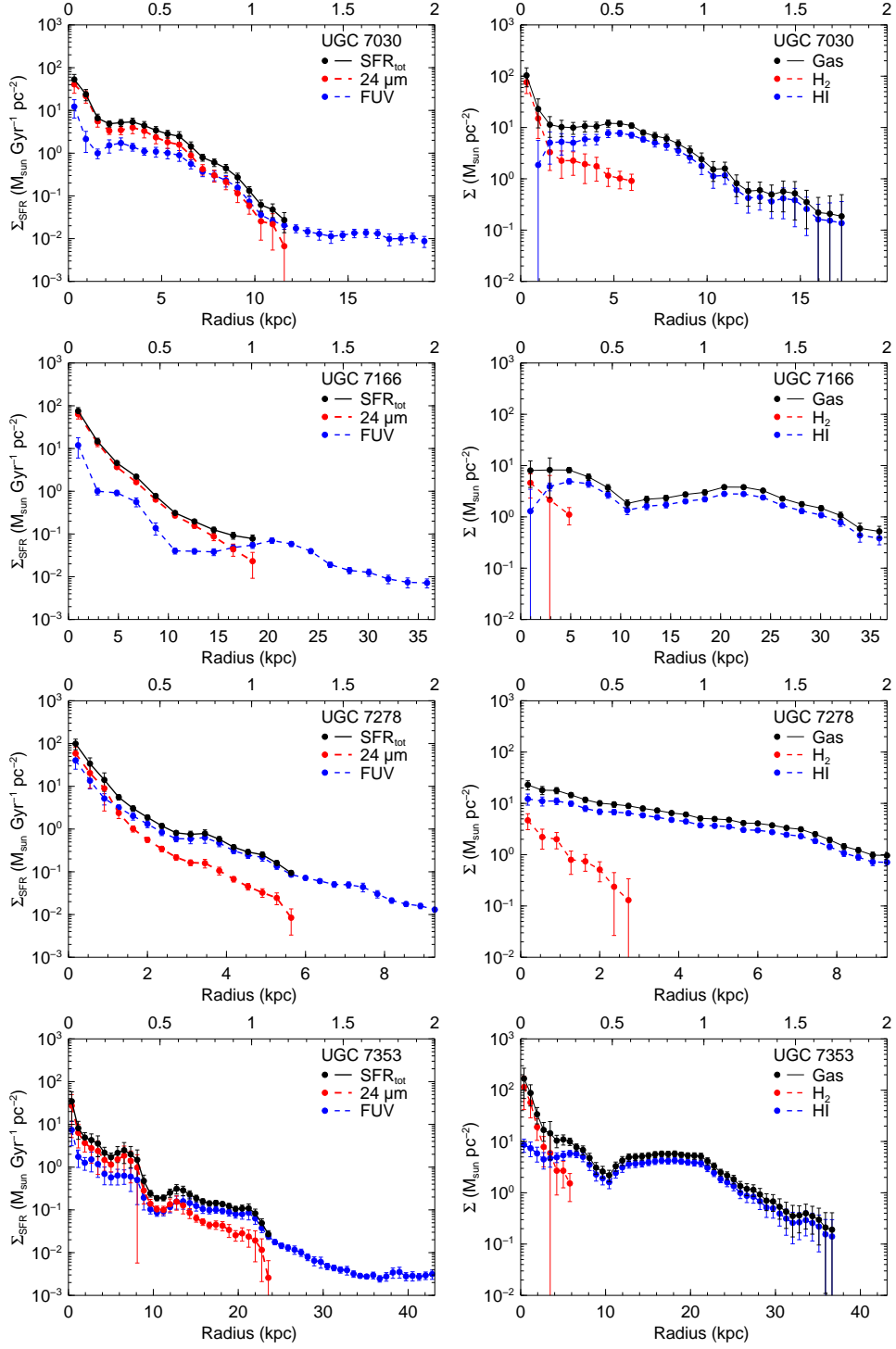


Figure 2. continued

tion (4) to compare with our scaling relation:

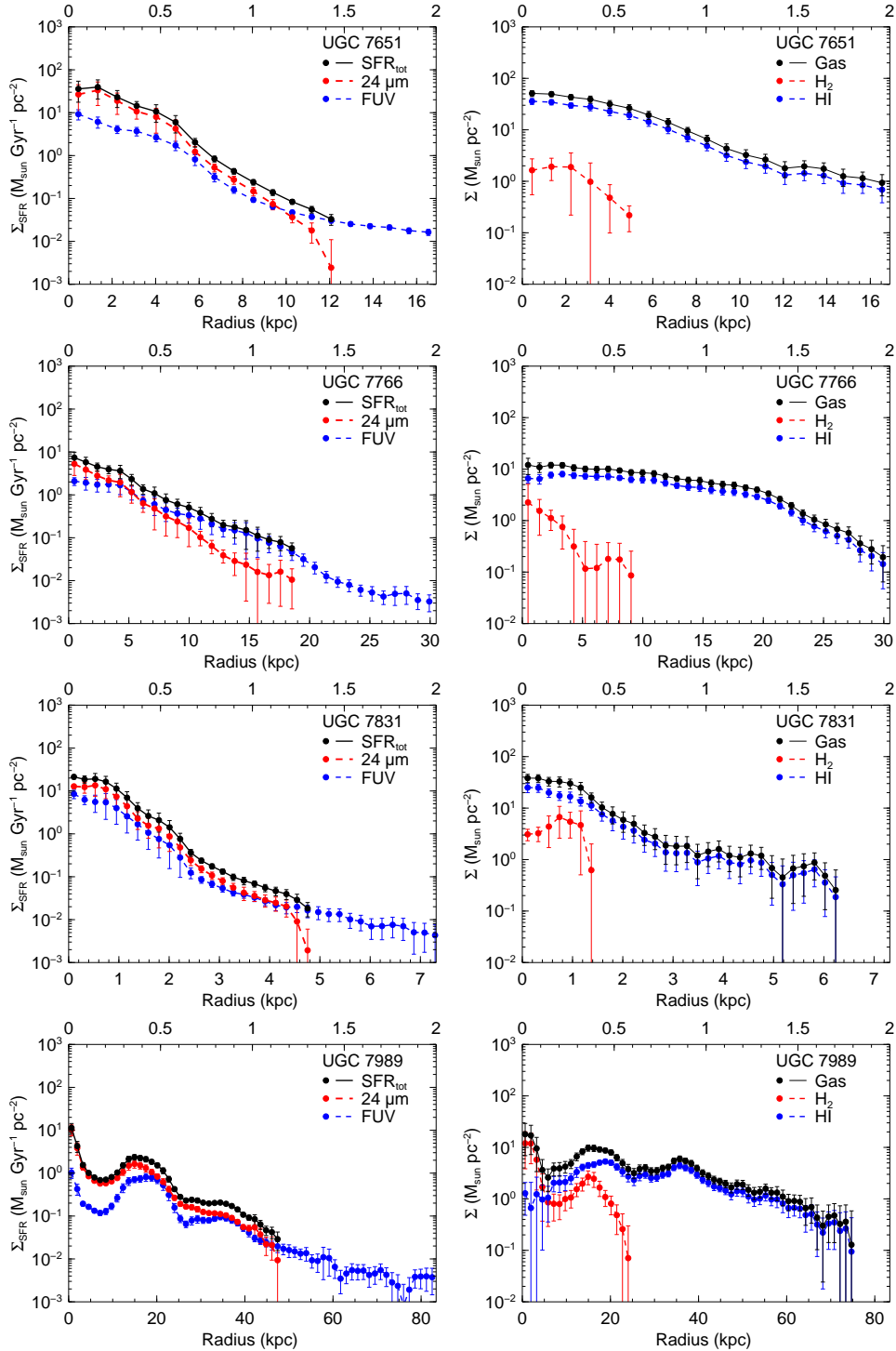
$$\Sigma_{\text{gas}} = 30.3 \times e^{-1.92 \times r/r_{25}}. \quad (5)$$

In this equation, which is obtained from the fit to our sample, we do not use Σ_{tr} to normalize Σ_{gas} since it is not possible to determine the value for several galaxies that do not have CO data or the transition radius. We also fitted the exponential function separately to only symmetric galaxies and asymmetric (including A/S) galaxies

to examine differences in the scaling relation. The scale lengths are 0.56 and 0.52 for the symmetric and asymmetric galaxies, respectively; so not significantly different.

4.3 Star Formation in the Inner Regions

Using the sub-sample with both CO and H I data (16 galaxies), we have examined the K-S law by plotting Σ_{SFR} against Σ_{H_2} and

**Figure 2.** continued

Σ_{gas} in the inner regions (within r_{25}) for the symmetric (red circles), A/S (purple octagons), asymmetric (blue squares), and interacting (light blue diamonds) galaxies in Figure 4 (top panels) to investigate whether the correlation is stronger in the asymmetric galaxies (including intermediate galaxies), suggesting a connection between star formation and gas accretion since we assume that asymmetric galaxies are subject to gas accretion. Note that the asymmetric group includes the intermediate (A/S) galaxies in

this section since (1) there is only one galaxy (UGC 7989) in the asymmetric group with CO and (2) the asymmetric and A/S galaxies are not significantly different from each other in their kinematics. However, we indicated each type of galaxy by different symbols in the figures. For the purposes of increasing the sample size and comparing with other observations, we included 12 THINGS (Walter et al. 2008) galaxies with CO data from Leroy et al. (2008). The THINGS sample consists of 8 symmetric, 3 slightly asymmet-

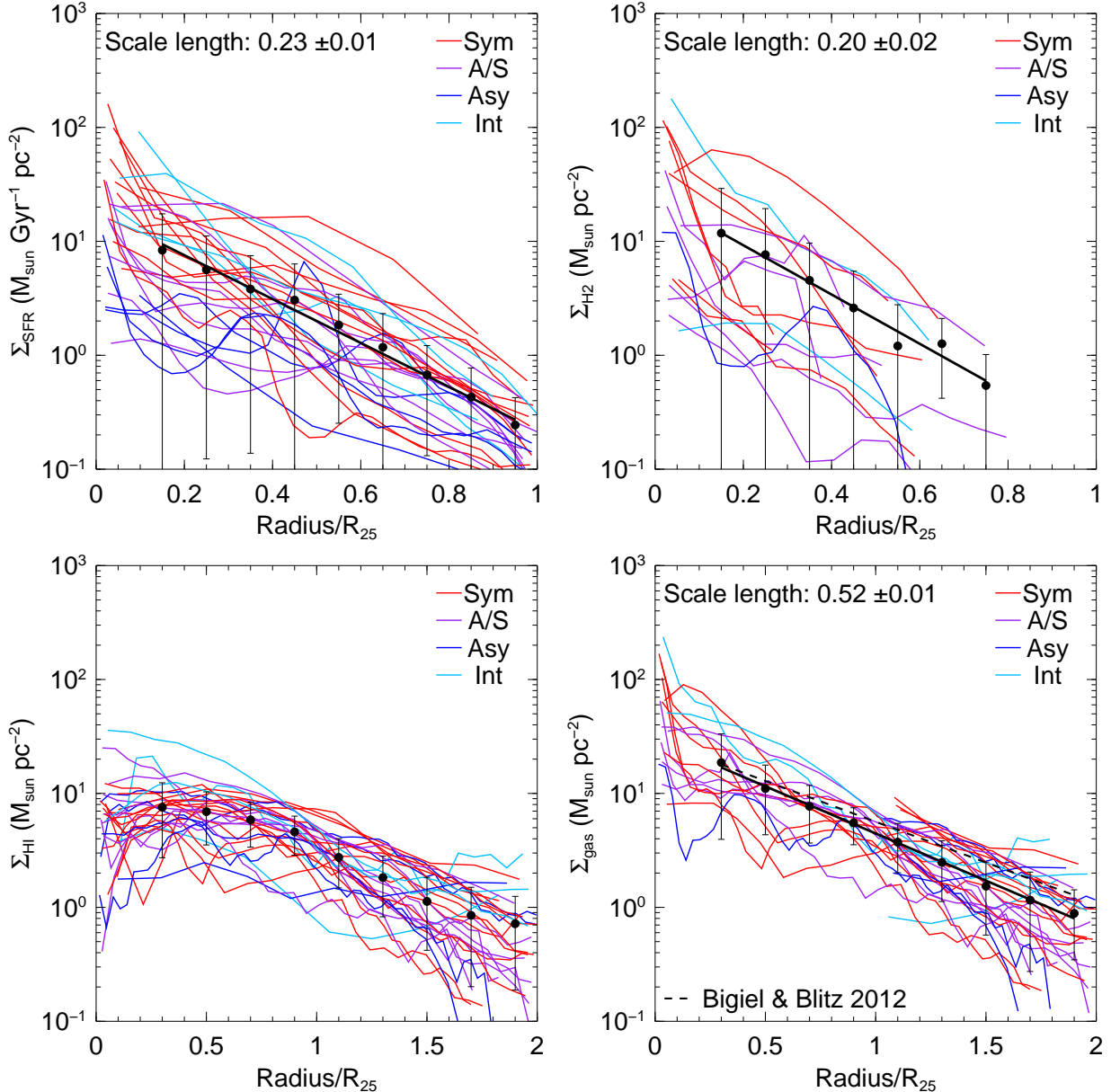


Figure 3. The scaled radial profiles of Σ_{SFR} (top left), Σ_{H_2} (top right), Σ_{HI} (bottom left), and Σ_{gas} (bottom right) for the symmetric (red), A/S (purple), asymmetric (blue), and interacting (light blue) galaxies. The filled circles are the average values in each bin ($0.2 \times r_{25}$) and the solid line is the exponential fit to the points. The dashed line in the bottom right panel is the fit given by Bigiel & Blitz (2012).

ric (A/S), and one interacting galaxy. They are plotted as open symbols (but the same symbol shape as the classes of our sample) in the figure. The THINGS galaxies show the same overall behaviour as the galaxies from the WHISP sample, and inclusion of these galaxies does not alter the lack of any significant difference between the galaxy classes. We used the ordinary least-squares (OLS) bisector (Isobe et al. 1990) to fit Σ_{SFR} vs. Σ_{H_2} and Σ_{gas} in logarithmic space for each galaxy. The power-law index (N) shown in the figure is the average value of the all galaxies, while the indices $N_{\text{A+AS}}$, N_{I} , and N_{S} represent the average values of the asymmetric (including A/S), interacting, and symmetric groups, respectively. Although the average indices are clearly different for the three groups and some symmetric galaxies seem to exhibit a weak correlation in the regions where Σ_{SFR} and Σ_{gas} values are higher, we do not see a much tighter correlation among the groups. In the top right panel

of Figure 4, the relation of SFR surface density versus total gas density is slightly steeper for the asymmetric galaxies as compared to the symmetric galaxies, though the difference is hardly significant. The individual plots of Σ_{SFR} vs. Σ_{HI} , Σ_{H_2} , and Σ_{gas} for each galaxy are presented in Figure A2.

In the bottom panels of Figure 4, we show the star formation efficiency (SFE) for molecular gas ($\text{SFE}_{\text{H}_2} = \Sigma_{\text{SFR}}/\Sigma_{\text{H}_2}$) and total gas ($\text{SFE}_{\text{gas}} = \Sigma_{\text{SFR}}/\Sigma_{\text{gas}}$) as a function of radius normalized by the optical radius r_{25} . Like previous studies (e.g., Rownd & Young 1999; Leroy et al. 2008), the SFE_{H_2} is roughly constant although the scatter is somewhat large. On the other hand, the SFE_{gas} is decreasing with radius and the scatter is small except the inner region within $0.2 \times r_{25}$. The scatter in the total gas is reduced by a factor of 10, suggesting that the inclusion of H I in the SFE provides more

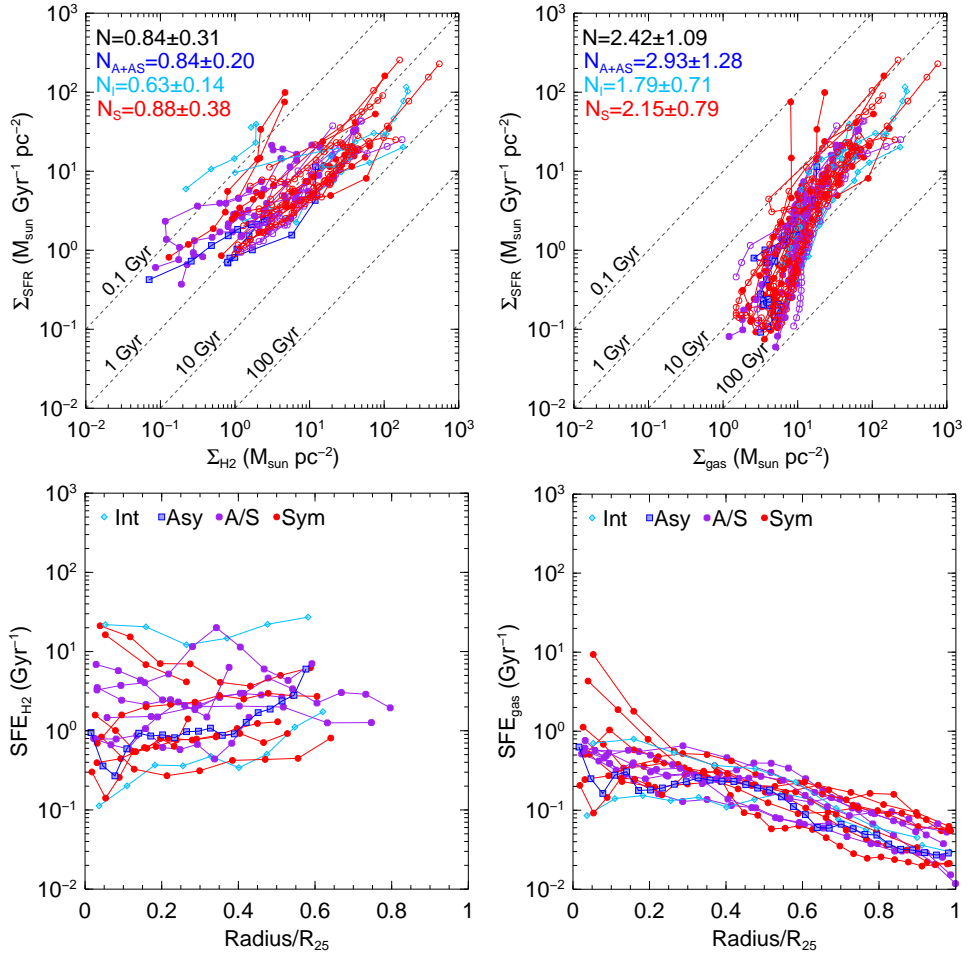


Figure 4. Top panels: Σ_{SFR} versus Σ_{H_2} (left) and Σ_{gas} (right). The average K-S indices are presented as N for all the galaxies, $N_{\text{A+S}}$ for the asymmetric and A/S galaxies, N_I for the interacting galaxies, and N_S for the symmetric galaxies. The different symbols indicate the different galaxy classes; light blue diamonds (interacting), blue squares (asymmetric), purple octagons (A/S), and red circles (symmetric) for the WHISHP galaxies (filled symbols) and the THINGS galaxies (open symbols). Bottom panels: SFE of the molecular gas ($\Sigma_{\text{SFR}}/\Sigma_{\text{H}_2}$) and SFE of the total gas ($\Sigma_{\text{SFR}}/\Sigma_{\text{gas}}$) as a function of radius normalized by the optical radius r_{25} .

meaningful results. Again, there is no significant difference among the groups.

4.4 Star Formation in the Outer Regions

Star formation in galaxies does not always stop at r_{25} or at the edge of the molecular gas disc, as demonstrated by the extended galactic discs in UV (e.g., Thilker et al. 2005; Gil de Paz et al. 2005). Bigiel et al. (2010) found a strong correlation between H I and FUV in the outer discs of many nearby spiral and dwarf galaxies. Since we are interested in a correlation between gas accretion and star formation, we also investigate a possible relationship between H I and FUV, especially in the outer regions where both H I and FUV extend to $2 \times r_{25}$ or more and where the effects of accretion may be most severe. Here, the outer regions are defined as $r > r_{25}$. Following the suggestion by Bigiel et al. (2010), we do not consider the internal extinction in FUV since the extinction correction may cause large uncertainties at the outer regions where S/N is low and background sources may contaminate FUV emission. In addition, the extinction effect would not be significant in the outer regions. Bigiel et al. (2010) estimated the internal extinction using a typical

value of H I column density at the outer discs; the correction factor is about 1.3.

Figure 5 shows Σ_{SFR} versus Σ_{HI} in the outer regions and SFE_{HI} ($= \Sigma_{\text{SFR}}/\Sigma_{\text{HI}}$) versus radius in units of r_{25} for symmetric (red circles), intermediate A/S (purple octagons), asymmetric (blue squares), and interacting (light blue diamonds) galaxies. For estimating Σ_{SFR} in the figure, we used the FUV term in Equation (1) since the $24 \mu\text{m}$ emission is negligible and the Σ_{SFR} profile is dominated by FUV in the outer regions. Unlike for the inner regions, a tight correlation between Σ_{SFR} and Σ_{HI} has been found in the outer regions for all the groups, although the scatter increases toward lower Σ_{HI} . We obtained the average K-S index of 1.21 using the OLS fit to Σ_{SFR} (from only FUV) vs. Σ_{HI} in the outer regions.

The very discrepant galaxy in the figures is the interacting galaxy UGC 4862 which has two tidal tails (Torres-Flores et al. 2012). The most prominent tail in the outer regions is masked in H I and FUV images when driving radial profiles. The H I profile shows very low density in the outer regions, especially near the optical radius, compared to other galaxies. The H I gas may be swept out toward the tail during interacting process, causing the low Σ_{HI} in the regions. On the other hand, the FUV profile shows much higher SFR near the radius of $2 \times r_{25}$ than that of other galaxies. The high

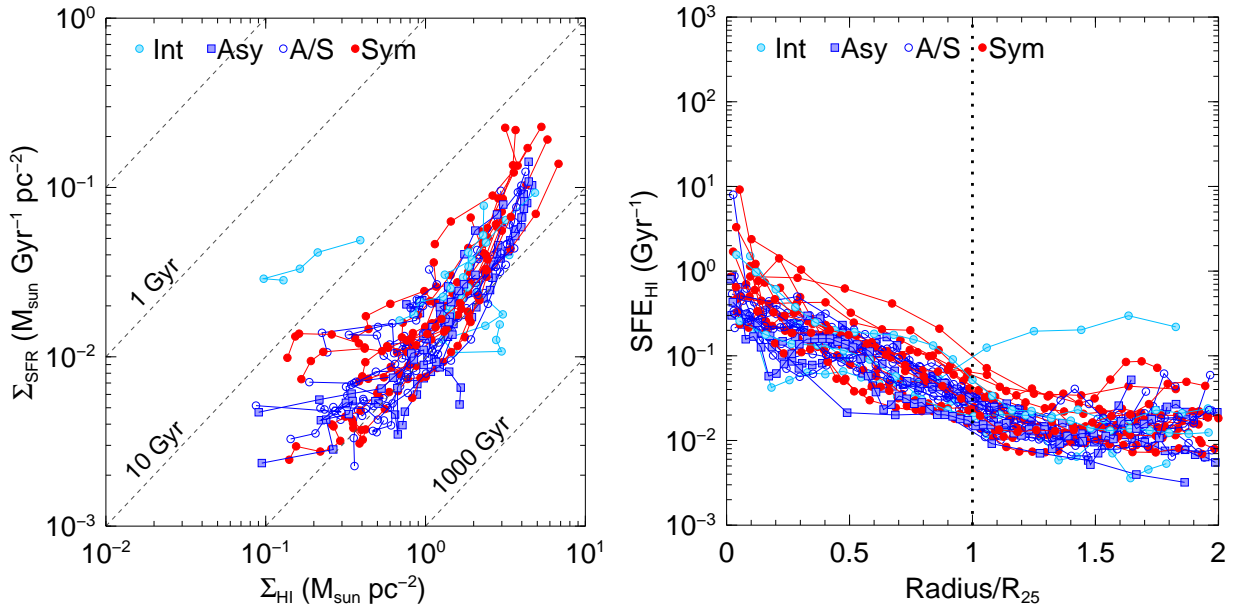


Figure 5. Σ_{SFR} versus Σ_{HI} (left) in the outer regions ($r_{25} - 2 \times r_{25}$) and SFE_{HI} with radius normalized by r_{25} (right). The vertical dotted line represents where $r = r_{25}$.

SFR in the outer regions might be linked to an extended UV (XUV) (Thilker et al. 2007) of this galaxy.

The right panel in the figure shows the SFE_{HI} decreasing (roughly exponentially) with radius up to $\sim 1.5 \times r_{25}$ and flattening (or roughly constant) beyond the radius. All galaxies in our sample appear to behave the same, so apparently the outer discs have very low SFE but also are extremely self regulating, probably because the H₁ surface density is very close to the critical density. In the end, it tells us more about galaxies than about how they get their gas. The roughly constant SFE in the outer regions agrees well with Bigiel et al. (2010), reinforcing the notion that the outer disks of spiral and irregular galaxies behave in a similar way, with low but constant star formation efficiencies. Why the outer disks behave this way is not yet very clear. Wong et al. (2016) building on the results of Meurer et al. (2013) and Zheng et al. (2013) show that for a model galaxy with constant Q the SFE declines toward r_{25} and becomes approximately constant in the outer parts. As discussed by Bigiel et al. (2010), this suggests that in the outer parts the disks are overall Q-stable while locally a small fraction of the gas clouds become unstable and form stars. Several studies have shown that the radial gradient of metallicity abundance is flat in the outer disks (e.g., Bresolin et al. 2009; Goddard et al. 2011). This flat gradient may be related to the constant SFE_{HI} in the outer regions. Like in the inner parts, we do not find a significant difference between the three groups of galaxies.

4.5 Dependence on the total stellar mass

Star formation depends on the total stellar mass (e.g., Noeske et al. 2007; Davé 2008). For this reason, there may be differences between the galaxy classes in the SF law (SFL) and SFE for different stellar mass ranges. We therefore re-examine the SFL and SFE, dividing the galaxies into specific stellar mass groups. To investigate this, we first estimated the total stellar mass (M_*) using the

Spitzer IRAC 3.6 and 4.5 μm maps following Eskew et al. (2012):

$$M_* = 10^{5.65} F_{3.6}^{2.85} F_{4.5}^{-1.85} \left(\frac{D}{0.05} \right)^2, \quad (6)$$

where $F_{3.6}$ and $F_{4.5}$ are fluxes of 3.6 and 4.5 μm in units of Jy and D is the distance in units of Mpc. Bright foreground stars in the maps are blanked. we used the MIRIAD tasks CGCURS and HISTO to define regions of galaxies and to integrate the galaxies, respectively. The estimated stellar masses for our sample are presented in Table 1. Figure 6 shows that the galaxies in our sample lie on the relation between star formation and stellar mass. The total SFR values are estimated by integrating the SFR surface density. The discrepant point in the lower right corner is the asymmetric galaxy UGC 7256 (NGC 4203) with low SFR. It is the only early type galaxy (S0) in our sample.

We grouped our sample of galaxies into three bins of the stellar mass: less massive than $10^{10} M_{\odot}$, intermediate, and more massive than $10^{11} M_{\odot}$. After comparing the galaxy classes in the same bins for the SFL and SFE, we noticed that there are still no differences between the symmetric, asymmetric, and interacting classes except that SFE_{HI} of the asymmetric and slightly asymmetric galaxies appears lower than that of the isolated symmetric galaxies when $M_* < 10^{10} M_{\odot}$ (see the left panel of Figure 7). The implication is that interactions suppress the SFE or increase the gas reservoir without enhancing the SF. To verify if the asymmetric galaxies with $M_* < 10^{10}$ are gas rich, we plotted the ratio of the total H₁ mass to the total stellar mass against M_* in Figure 7 (right). It appears that the symmetric galaxies below a stellar mass of $10^{10} M_{\odot}$ are systematically less gas rich than the asymmetric galaxies. The reason why the asymmetric galaxies are more gas rich is possibly due either to really lower SFE or the accretion of fresh gas.

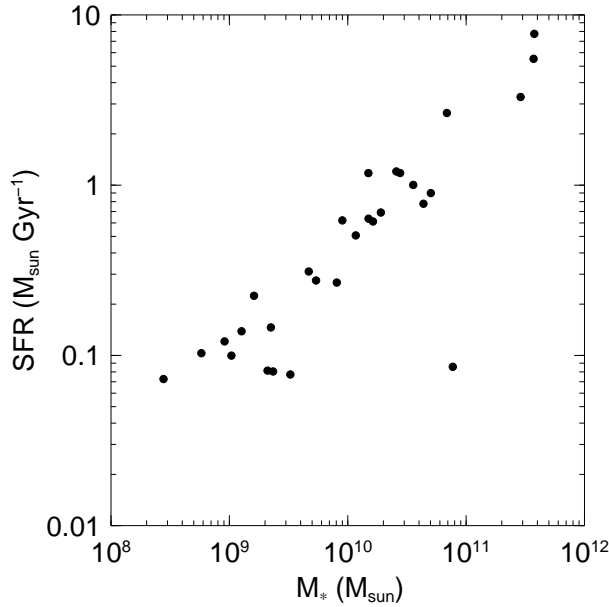


Figure 6. Total SFR versus M_* for the sample of galaxies.

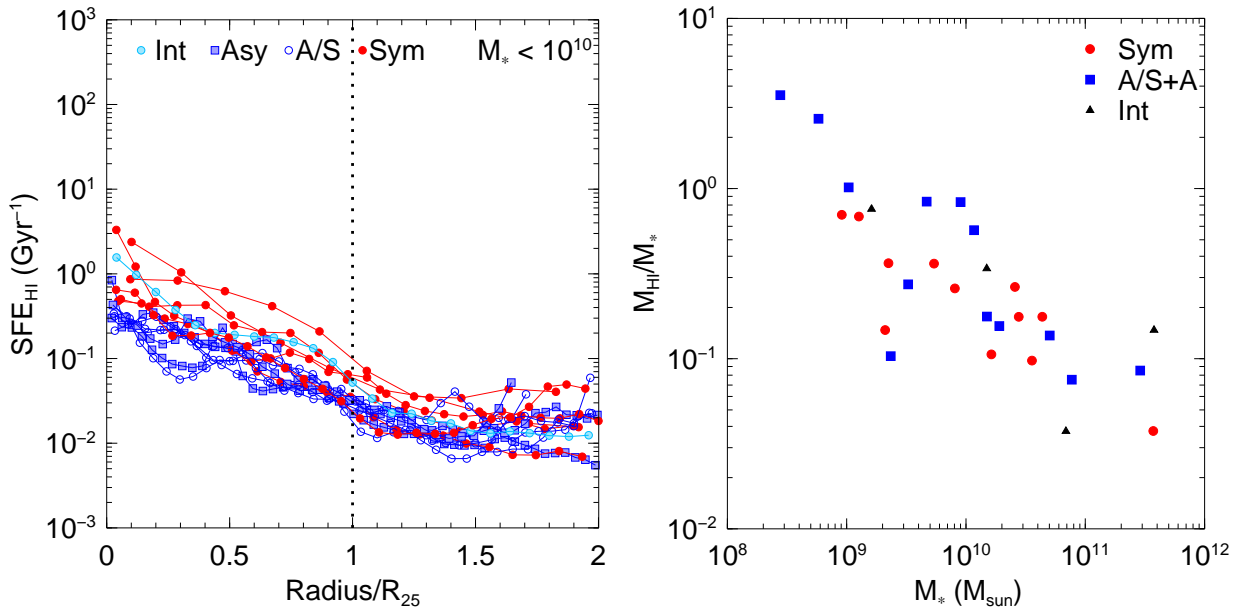


Figure 7. Left: SFE_{HI} as a function of r/r_{25} when the total stellar mass M_* is less than $10^{10} M_\odot$. The vertical dotted line represents where $r = r_{25}$. Right: the ratio of the total H I mass to the total stellar mass (M_{HI}/M_*) versus M_* in units of solar mass.

5 SUMMARY AND CONCLUSIONS

In order to find evidence for a positive correlation between gas accretion and star formation, we investigated the K-S law in the inner and outer regions (separately) with symmetric, asymmetric, and interacting groups of galaxies and compared them to each other. In addition, we compared the scaled radial profiles of Σ_{SFR} , Σ_{H_2} , Σ_{HI} , and Σ_{gas} for the groups to see if there is any difference between them.

1. Among the sub-sample of 16 galaxies with both CO and H I data, several galaxies show Σ_{H_2} lower than Σ_{HI} in the central regions unlike the general trend of CO and H I radial profiles

demonstrating that the molecular gas density is higher than the H I density near the center.

2. The scaled radial profiles of the total gas are well constrained by the exponential fit regardless of the galaxy types. There is no significant difference between symmetric and asymmetric galaxy groups and the scale lengths are 0.56 (symmetric) and 0.52 (asymmetric).

3. The examination for the K-S law in the inner regions exhibits no tighter correlation among the symmetric and asymmetric groups of galaxies and no clear sign for a relationship between gas accretion and star formation. However, the power-law correlation of some symmetric galaxies appears somewhat weaker than that of

the asymmetric and interacting galaxies, especially in the central regions where Σ_{SFR} and Σ_{gas} are higher. The average indices for the molecular K-S law are 0.84 (asymmetric) and 0.88 (symmetric). The indices for the total gas are 2.93 (asymmetric) and 2.15 (symmetric). The SFE for the molecular gas is roughly constant with radius while the SFE for the total gas decreases with radius for both the symmetric and asymmetric galaxies.

4. From the plot of Σ_{SFR} vs. Σ_{HI} for the outer regions beyond r_{25} , we noticed that there is a tight correlation between SFR and H I in the outer discs unlike in the inner regions. The average K-S index for all the galaxies is 1.21. The SFE_{HI} decreases (roughly exponentially) until $1.5 \times r_{25}$ and flattens beyond that radius. There is no significant difference between the galaxy groups for the SFL and SFE except that the isolated symmetric galaxies with small stellar mass ($< 10^{10} M_{\odot}$) have somewhat higher SFE.

ACKNOWLEDGEMENTS

We thank the anonymous referee for useful suggestions that improved this paper. The research leading to these results has received funding from the European Research Council under the European Union's Seventh Framework Programme (FP/2007-2013) / ERC Grant Agreement nr. 291531.

REFERENCES

- Baldwin J. E., Lynden-Bell D., Sancisi R., 1980, MNRAS, **193**, 313
 Bigiel F., Blitz L., 2012, ApJ, **756**, 183
 Bigiel F., Leroy A., Walter F., Brinks E., de Blok W. J. G., Madore B., Thornley M. D., 2008, AJ, **136**, 2846
 Bigiel F., Leroy A., Walter F., Blitz L., Brinks E., De Blok W. J. G., Madore B., 2010, The Astronomical Journal, 140, 1194
 Binney J., Dehnen W., Bertelli G., 2000, MNRAS, **318**, 658
 Bournaud F., Combes F., Jog C. J., Puerari I., 2005, A&A, **438**, 507
 Bresolin F., Ryan-Weber E., Kennicutt R. C., Goddard Q., 2009, ApJ, **695**, 580
 Brooks A. M., Governato F., Quinn T., Brook C. B., Wadsley J., 2009, The Astrophysical Journal, 694, 396
 Calzetti D., et al., 2007, ApJ, **666**, 870
 Combes F., et al., 2009, A&A, **503**, 73
 Dame T. M., Hartmann D., Thaddeus P., 2001, ApJ, **547**, 792
 Davé R., 2008, MNRAS, **385**, 147
 Dekel A., et al., 2009, Nature, 457, 451
 Elmegreen D. M., Salzer J. J., 1999, AJ, **117**, 764
 Epinat B., Amram P., Marcelin M., 2008, MNRAS, **390**, 466
 Eskew M., Zaritsky D., Meidt S., 2012, AJ, **143**, 139
 Frernali F., Tomasetti M., 2012, MNRAS, **426**, 2166
 García-Burillo S., et al., 2003, in Collin S., Combes F., Shlosman I., eds, Astronomical Society of the Pacific Conference Series Vol. 290, Active Galactic Nuclei: From Central Engine to Host Galaxy. p. 423 (arXiv:astro-ph/0212451)
 Gil de Paz A., et al., 2005, ApJ, **627**, L29
 Gil de Paz A., et al., 2007, ApJS, **173**, 185
 Goddard Q. E., Bresolin F., Kennicutt R. C., Ryan-Weber E. V., Rosales-Ortega F. F., 2011, MNRAS, **412**, 1246
 Helfer T. T., Thornley M. D., Regan M. W., Wong T., Sheth K., Vogel S. N., Blitz L., Bock D. C.-J., 2003, ApJS, **145**, 259
 Isobe T., Feigelson E. D., Akritas M. G., Babu G. J., 1990, Astrophysical Journal, 364, 104
 Jog C. J., 1997, ApJ, **488**, 642
 Kamphuis J. J., Sijbring D., van Albada T. S., 1996, A&AS, **116**, 15
 Kennicutt Jr. R. C., 1983, ApJ, **272**, 54
 Kennicutt Jr. R. C., 1998, ApJ, **498**, 541
 Kennicutt R. C. J., et al., 2003, The Publications of the Astronomical Society of the Pacific, 115, 928
 Kennicutt Jr. R. C., et al., 2007, ApJ, **671**, 333
 Larson R. B., Tinsley B. M., Caldwell C. N., 1980, ApJ, **237**, 692
 Leroy A. K., Walter F., Brinks E., Bigiel F., de Blok W. J. G., Madore B., Thornley M. D., 2008, AJ, **136**, 2782
 Leroy A. K., et al., 2009, AJ, **137**, 4670
 Leroy A. K., et al., 2012, AJ, **144**, 3
 Mapelli M., Moore B., Bland-Hawthorn J., 2008, MNRAS, **388**, 697
 Matthews L. D., Uson J. M., 2008, AJ, **135**, 291
 Meurer G. R., Zheng Z., de Blok W. J. G., 2013, MNRAS, **429**, 2537
 Noeske K. G., et al., 2007, ApJ, **660**, L43
 Noordermeer E., 2006, PhD thesis, Groningen: Rijksuniversiteit
 Noordermeer E., van der Hulst J. M., Sancisi R., Swaters R. A., van Albada T. S., 2005, A&A, **442**, 137
 Odewahn S. C., 1991, AJ, **101**, 829
 Oosterloo T., Frernali F., Sancisi R., 2007a, The Astronomical Journal, 134, 1019
 Oosterloo T. A., Morganti R., Sadler E. M., van der Hulst T., Serra P., 2007b, Astronomy and Astrophysics, 465, 787
 Ostriker E. C., Binney J. J., 1989, MNRAS, **237**, 785
 Rahman N., et al., 2011, ApJ, **730**, 72
 Richter O.-G., Sancisi R., 1994, A&A, **290**, L9
 Rownd B. K., Young J. S., 1999, AJ, **118**, 670
 Salim S., et al., 2007, ApJS, **173**, 267
 Sánchez Almeida J., Elmegreen B. G., Muñoz-Tuñón C., Elmegreen D. M., 2014, The Astronomy and Astrophysics Review, 22, 71
 Sancisi R., Frernali F., Oosterloo T., van der Hulst T., 2008, The Astronomy and Astrophysics Review, 15, 189
 Schlegel D. J., Finkbeiner D. P., Davis M., 1998, The Astrophysical Journal, 500, 525
 Strong A. W., Mattox J. R., 1996, A&A, **308**, L21
 Swaters R. A., 1999, PhD thesis, , Rijksuniversiteit Groningen, (1999)
 Swaters R. A., van Albada T. S., van der Hulst J. M., Sancisi R., 2002, A&A, **390**, 829
 Thilker D. A., et al., 2005, The Astrophysical Journal, 619, L79
 Thilker D. A., et al., 2007, ApJS, **173**, 538
 Torres-Flores S., de Oliveira C. M., de Mello D. F., Scarano S., Urrutia-Viscarra F., 2012, MNRAS, **421**, 3612
 Twarog B. A., 1980, ApJ, **242**, 242
 Wakker B. P., York D. G., Wilhelm R., Barentine J. C., Richter P., Beers T. C., Ivezić Ž., Howk J. C., 2008, ApJ, **672**, 298
 Walter F., Brinks E., de Blok W. J. G., Bigiel F., Kennicutt Jr. R. C., Thornley M. D., Leroy A., 2008, AJ, **136**, 2563
 Wong T., Blitz L., 2002, ApJ, **569**, 157
 Wong T., et al., 2013, ApJ, **777**, L4
 Wong O. I., Meurer G. R., Zheng Z., Heckman T. M., Thilker D. A., Zwaan M. A., 2016, MNRAS, **460**, 1106
 Wyder T. K., et al., 2007, The Astrophysical Journal Supplement Series, 173, 293
 Young J. S., et al., 1995, ApJS, **98**, 219
 Zaritsky D., Rix H.-W., 1997, ApJ, **477**, 118
 Zheng Z., Meurer G. R., Heckman T. M., Thilker D. A., Zwaan M. A., 2013, MNRAS, **434**, 3389
 de Vaucouleurs G., de Vaucouleurs A., Corwin Jr. H. G., Buta R. J., Paturel G., Fouqué P., 1991, Third Reference Catalogue of Bright Galaxies. Volume I: Explanations and references. Volume II: Data for galaxies between 0^h and 12^h . Volume III: Data for galaxies between 12^h and 24^h .
 van Eymeren J., Jütte E., Jog C. J., Stein Y., Dettmar R.-J., 2011a, A&A, **530**, A29
 van Eymeren J., Jütte E., Jog C. J., Stein Y., Dettmar R.-J., 2011b, A&A, **530**, A30
 van der Hulst T., Sancisi R., 2004, International Astronomical Union Symposium no. 217, 217, 122
 van der Hulst J. M., Terlouw J. P., Begeman K. G., Zwitser W., Roelfsema P. R., 1992, in Worrall D. M., Biemesderfer C., Barnes J., eds, Astro-

nomical Society of the Pacific Conference Series Vol. 25, Astronomical Data Analysis Software and Systems I. p. 131
van der Hulst J. M., van Albada T. S., Sancisi R., 2001, in Hibbard J. E., Rupen M., van Gorkom J. H., eds, Astronomical Society of the Pacific Conference Series Vol. 240, Gas and Galaxy Evolution. p. 451

This paper has been typeset from a $\text{\TeX}/\text{\LaTeX}$ file prepared by the author.

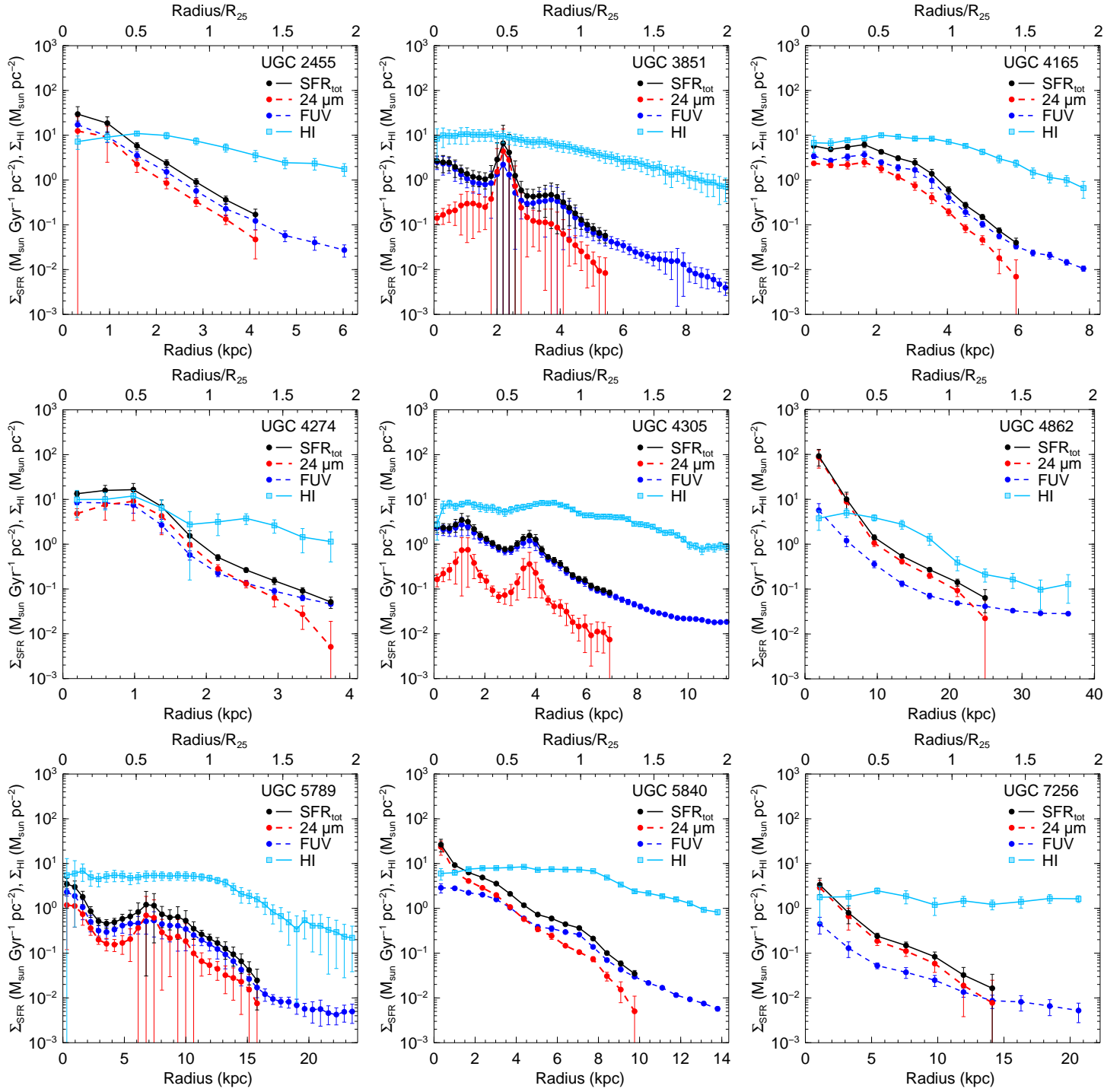
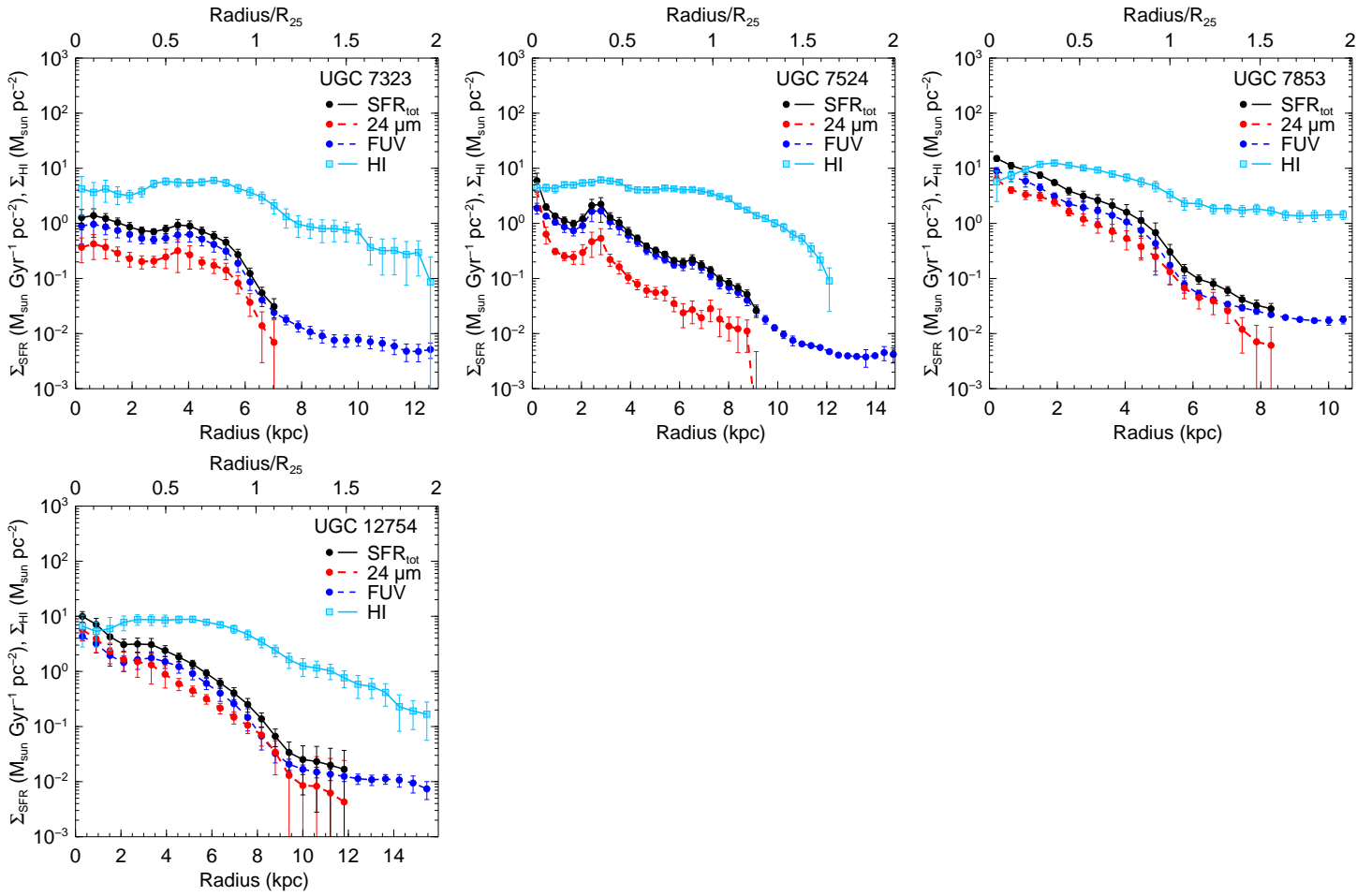


Figure A1. SFR and HI surface densities as a function of radius for 13 galaxies that have no CO data.

**Figure A1.** continued

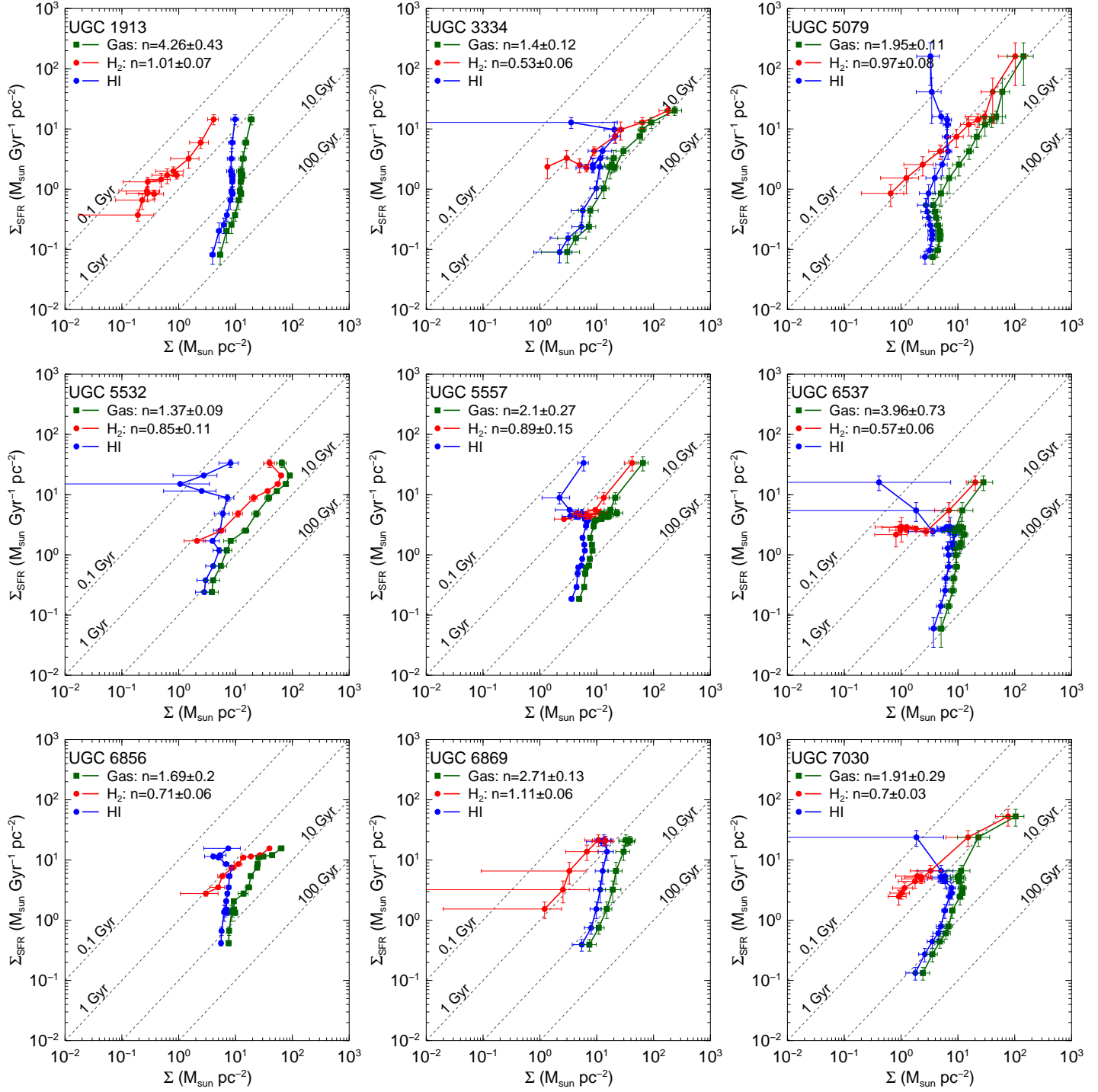
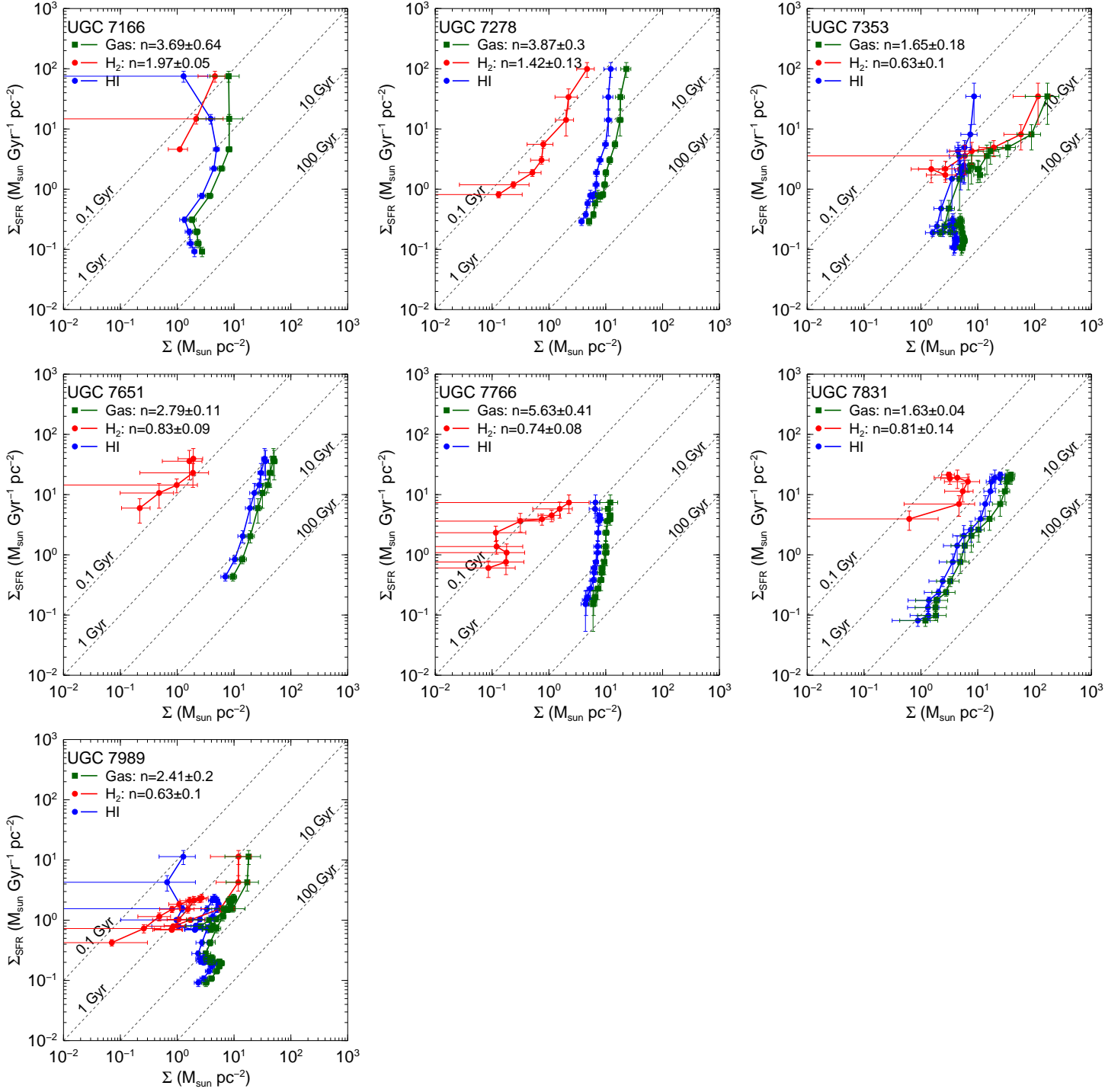


Figure A2. SFR surface density as a function of H_2 (red), HI (blue), and total gas (green) surface densities for the sub-sample of 16 galaxies with CO data.

**Figure A2.** continued